ADVANCED ELECTRONIC MATERIALS
www.advelectronicmat.de

Enhancement of the Magnetoresistance in the Mobility-Engineered Compensated Metal Pt_5P_2

Alex H. Mayo, Hidefumi Takahashi, Shintaro Ishiwata, Karolina Górnicka, Michał J. Winiarski, Jan Jaroszynski, Robert J. Cava, Weiwei Xie, and Tomasz Klimczuk**

The magnetoresistance (MR) in nonmagnetic materials continues to be a fertile research area in materials science. The search for giant, positive MR has been limited to a rather small window of materials such as high-mobility semimetals in single-crystalline form. Here, the observation of a very large positive MR in metallic Pt_5P_2 in polycrystalline form is reported. The observations reveal that improvement of the crystallinity results in a significant enhancement of the positive MR, exceeding 10 000% at 9 T, comparable to high-mobility semimetals. Based on first-principles calculations combined with magnetotransport and thermoelectric measurements, the Fermi surface of Pt_5P_2 is found to consist of a collection of multiple electron and hole pockets compensating one another, along with a characteristic pocket continuously connected to the adjacent Brillouin zone, together with possible topologically protected band crossings. This work extends the landscape of high MR candidate materials to polycrystalline metals, which demonstrates the importance of crystallinity and purity of the samples for the optimization of the MR.

1. Introduction

Conduction electrons in a solid show orbital motion under transverse magnetic fields, which manifests itself as a positive magnetoresistance (MR) in nonmagnetic multicarrier systems. This positive MR becomes significantly large in high-mobility semiconductors and semimetals,[1–4] especially in topological semimetals.[5–9] For instance in WTe_2, a large positive MR without saturation at high magnetic fields has been observed, reflecting the small effective mass and nearly perfect compensation of the electron and hole carriers.[5] Since the classical orbital MR in multicarrier systems is proportional to $(\mu B)^2$, where μ is the carrier mobility and B is a magnetic field, considerable attention has been paid to high-mobility semiconductors and semimetals as materials with a giant MR. On the other hand, metallic systems with a large carrier density have been overlooked, as the carrier mobility tends to be reduced by the intrinsic electron–electron scattering displayed by materials with large or multiple Fermi surfaces. From the viewpoint of materials engineering, due to the fact that charge mobility is degraded by the extrinsic scattering by impurity and grain boundaries, high-purity single crystals are typically considered more promising than polycrystals.[10,11]

Here, we focus on a metallic binary compound, Pt_5P_2, in a polycrystalline form. The crystal structure of Pt_5P_2 was

A. H. Mayo,[+] H. Takahashi, S. Ishiwata
Division of Materials Physics and Center for Spintronics Research Network (CSRN)
Graduate School of Engineering Science
Osaka University
Osaka 560-8531, Japan
E-mail: ishiwata@mp.es.osaka-u.ac.jp
A. H. Mayo
Department of Applied Physics
The University of Tokyo
Tokyo 113-8656, Japan

The ORCID identification number(s) for the author(s) of this article can be found under https://doi.org/10.1002/aelm.202201120.

© 2022 The Authors. Advanced Electronic Materials published by Wiley-VCH GmbH. This is an open access article under the terms of the Creative Commons Attribution License, which permits use, distribution and reproduction in any medium, provided the original work is properly cited.

[+]Present address: Institute for Materials Research, Tohoku University, Sendai 980-8577, Japan

DOI: 10.1002/aelm.202201120

K. Górnicka, M. J. Winiarski, T. Klimczuk
Faculty of Applied Physics and Mathematics
Gdańsk University of Technology
Narutowicza 11/12, Gdansk 80-233, Poland
E-mail: tomasz.klimczuk@pg.edu.pl
K. Górnicka, M. J. Winiarski, T. Klimczuk
Advanced Materials Center
Gdańsk University of Technology
Narutowicza 11/12, Gdansk 80-233, Poland
J. Jaroszynski
National High Magnetic Field Laboratory
1800 E. Paul Dirac Drive, Tallahassee, FL 32310, USA
R. J. Cava
Department of Chemistry
Princeton University
Princeton, NJ 08540, USA
W. Xie
Department of Chemistry
Michigan State University
Michigan, MI 48824, USA

 © 2022 The Authors. Advanced Electronic Materials published by Wiley-VCH GmbH

Check for updates
2199160x, 0, Downloaded from https://onlinelibrary.wiley.com/doi/10.1002/aelm.202201120 by Tomasz Klimczuk - Pcp/Technical University Of , Wiley Online Library on [30/12/2022]. See the Terms and Conditions (https://onlinelibrary.wiley.com/terms-and-conditions) on Wiley Online Library for rules of use; OA articles are governed by the applicable Creative Commons License

reported in 1967.[12] However, the physical properties, such as its electronic structure and transport properties, have not been explored so far. In the present work, we report details of the synthesis, crystal structure, resistivity, magnetotransport, and the Seebeck measurements of Pt_5P_2. We observe that improvement of the crystallinity in high-purity Pt_5P_2 polycrystalline samples results in a significant enhancement of the positive MR. On the basis of first-principles calculations and the transport measurements for several samples with different crystallinity, we find that metallic compounds with a complex band dispersion that involves topologically protected linear bands have a great potential to show an extremely large MR, even comparable to high-mobility semimetals in single-crystalline form.

2. Results

Pt_5P_2 crystallizes in a unique monoclinic structure ($C2/c$, no. 15) (**Figure 1**a,b), as reported by Dahl et al.[12] No isostructural compounds have been reported to date and the isoelectronic Pd_5Sb_2 features a completely different atomic network.[13] In the Pd–P system, a Pd_5P_2 phase has been reported to form,[14] but its crystal structure is not included in the inorganic crystal structure database.

In this project, we synthesized and studied six Pt_5P_2 samples (A–F) that are listed in Table S1 (Supporting Information). Figure 1c presents the powder X-ray diffraction (pXRD) pattern for sample A, whereas the pXRD pattern of sample B can be found in the Supporting Information. All of the diffraction peaks were assigned by the LeBail refinement (monoclinic $C/2c$ structure), revealing that the material is single phase. The inset to the figure shows a zoom between 39° and 42° in the vicinity of the expected Pt reflection, marked by an arrow, which indicates the absence of elemental Pt as an impurity down to the sensitivity of the diffraction experiment (a few percent). The details of structure refinement obtained by single crystal X-ray diffraction on sample A are provided in Tables S2–5 (Supporting Information).

The structure determination shows that the Pt atoms, occupying three independent crystallographic sites, form infinite chains of corner-sharing Pt_6 octahedra along the c-axis with nearest neighbor (NN) Pt–Pt distances within the chains ranging from 2.78 to 2.84 Å, slightly longer than in elemental Pt (2.77 Å[15]). The closest contacts between the chains are 2.80 and 2.85 Å (Pt2–Pt2 and Pt3–Pt3, respectively; both roughly along the a-axis), suggesting significant interchain interactions. P atoms (one independent site) fill the voids of the Pt framework, resulting in a slightly buckled honeycomb network, with NN P–P distances of ≈3.4 Å. Importantly, with such large separation, direct P–P bonding is expected to be negligible. This implies a significant difference from semiconducting or semimetallic Zintl binary phosphides[16–21] in that the Pt_6 octahedron breaks the covalent P–P bonding inherent in Zintl compounds and the system becomes highly metallic, comparable to elemental Pt as shown below.

Figure 1d,e shows scanning electron microscopy (SEM) pictures of the samples with high (sample A) and low (sample B) crystallinity, illustrating the dramatic difference in the material's microstructure dependent on the synthesis method employed. Sample A was prepared by melting and annealing a stoichiometric mixture of Pt and P, whereas sample B was made by a standard solid-state reaction method (for details—see Supporting Information). For both, the same source of Pt powder was used. The grain size in sample A reaches the order of ≈10 μm in contrast with much smaller grain size seen in sample B. Such large differences in grain size are expected to affect electronic transport due to scattering at the grain boundaries.

Figure 2 shows temperature dependencies of the electrical resistivity, Seebeck coefficient, and magnetotransport properties of Pt_5P_2. For A and B samples, a metallic-like character of resistivity ($d\rho/dT < 0$) is seen (Figure 2a). A detailed analysis of the resistivity together with a parallel resistor model fit for both samples are provided in the Supporting Information. Metallicity is consistent with the nonzero Sommerfeld coefficient ($\gamma = 7.2(1)$ mJ mol^{-1} K^{-2}) obtained from the low-temperature heat capacity data fit—see Figure S5b (Supporting Information). As anticipated from Figure 1d,e, sample A reveals a much larger residual resistivity ratio (RRR) of ≈370 compared with that of sample B (≈12). Moreover, sample A shows a large positive magnetoresistance (MR), exceeding 10 000% at 9 T (Figure 2b,c), despite the fact that it is not a single crystal. The MR decreases dramatically by three orders of magnitude for the low crystallinity sample B. For both samples, the MR decreases with increasing temperature and is close to unity above 80 K, which is seen as the overlap of $\rho(T)$ measured at 0 and 9 T. The field-dependent MR (sample A) at 1.85, 10, 15, and 20 K is presented in Figure 2b. A remarkable scaling with $\mu_0 H^n$ up to 9 T is observed with the exponent ($n = 1.79$) relatively close to an H^2 dependence. Sample A was also studied in high magnetic fields, and the data collected at 4 and 30 K are shown in panel d of Figure 2. At the lower temperature, the MR reaches 60 000% (30 T), and reveals clear nonsaturating behavior.

The temperature dependence of the Seebeck coefficient of sample A is shown in Figure 2e. The Seebeck coefficient $S(T)$ is fairly small in absolute value and shows a sign reversal at around 80 K, which is the same temperature at which the MR ≈1. Such behavior indicates that the sample is a metal, with both hole and electron pockets, with a large carrier density (i.e., large Fermi energy). This is consistent with the carrier density of ≈2.0×10^{22} cm^{-3} obtained from the linear fit of the Hall resistivity data presented in Figure 2f. Here, while the Hall resistivity shows nonlinear magnetic-field behavior reflecting a multicarrier nature, a linear fitting assuming a single-carrier model was employed to estimate the carrier density as shown by the blue line at low fields in Figure 2f. Further multicarrier analysis reconfirms the high carrier density and also the high degree of compensation between hole and electron carriers, as anticipated from $S(T)$—for details, see the Supporting Information.[22] The obtained carrier mobilities give ≈10^4 cm^2 V^{-1} s^{-1} (=1 m^2 V^{-1} s^{-1}) for both electrons and holes (Table S6, Supporting Information), which is a large value for a polycrystalline sample. Thus, the transport measurements suggest that Pt_5P_2 is a metal with high carrier mobility. A notable feature is an extremely large MR for a sample in polycrystalline form, an indication that this material has a special electronic structure.

Figure 3 shows a comparison of the MR at 9 T plotted against the conductivity at low temperature ($T \approx 2$ K) in zero-applied field among well-known metals and semimetals. The data for the materials besides Pt_5P_2 were taken from the literature.[5,6,8,11,23–30]

MOST WIEDZY Downloaded from mostwiedzy.pl

2199160x, 0, Downloaded from https://onlinelibrary.wiley.com/doi/10.1002/aelm.202201120 by Tomasz Klimczuk - Pcp/Technical University Of , Wiley Online Library on [30/12/2022]. See the Terms and Conditions (https://onlinelibrary.wiley.com/terms-and-conditions) on Wiley Online Library for rules of use; OA articles are governed by the applicable Creative Commons License

© 2022 The Authors. Advanced Electronic Materials published by Wiley-VCH GmbH

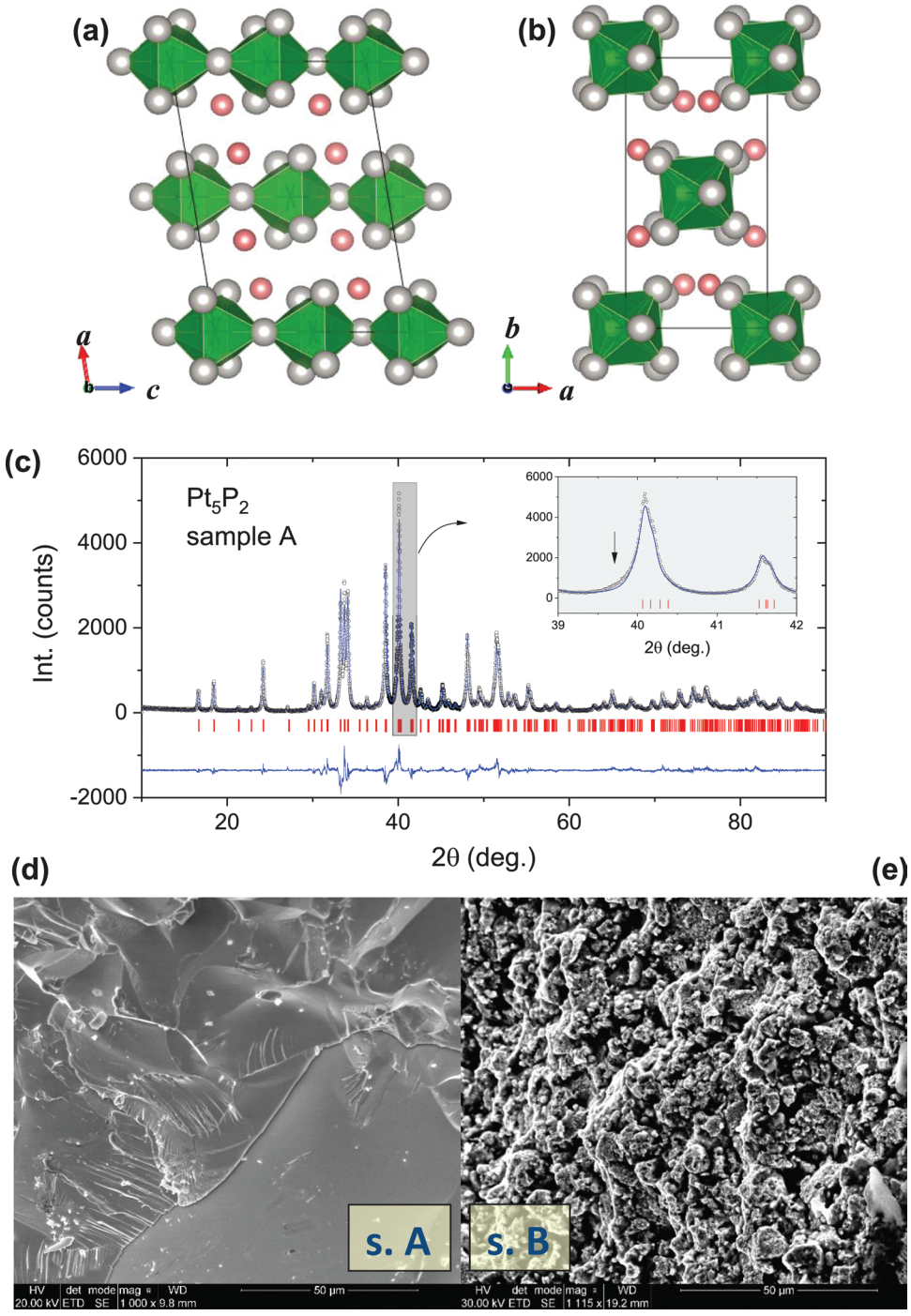

Figure 1. a,b) Crystal structure, c) powder XRD pattern with the LeBail refinement, and d,e) SEM images of Pt_5P_2. The red and gray balls represent phosphorus and platinum atoms, respectively. The inset in (c) shows the 39°–42° region in the vicinity of a strong expected elemental Pt reflection, marked by a vertical arrow. In (d) and (e), the sample with high and low crystallinity is referred to as samples A and B, respectively.

The MR of the five studied Pt_5P_2 samples with different crystallinity was found to increase systematically with increasing crystallinity. Note that the sixth sample (sample C) is a chemically doped $(Pt_{1.96}Ir_{0.04})_5P_2$ that reveals almost the same MR as a sample prepared by the solid-state reaction method (sample B).

The observed influence of the crystallinity level on the MR can be considered as being a result of a systematic change in the charge carrier mobility, μ. In the case of ideally compensated (semi-)metals (i.e., $n_e = n_h$), the MR is reduced to the following form:

$$\mathrm{MR}(B) = \frac{B^2 n_e n_h |\mu_e||\mu_h|\left(|\mu_e| + |\mu_h|\right)^2}{\left(|\mu_e| n_e + |\mu_h| n_h\right)^2 + \left(B^2 \mu_e^2 \mu_h^2 (n_e - n_h)^2\right)} = |\mu_e||\mu_h| B^2 \sim \mu^2 B^2 \quad (1)$$

© 2022 The Authors. Advanced Electronic Materials published by Wiley-VCH GmbH

MOST WIEDZY Downloaded from mostwiedzy.pl

2199160x, 0, Downloaded from https://onlinelibrary.wiley.com/doi/10.1002/aelm.202201120 by Tomasz Klimczuk - Pcp/Technical University Of , Wiley Online Library on [30/12/2022]. See the Terms and Conditions (https://onlinelibrary.wiley.com/terms-and-conditions) on Wiley Online Library for rules of use; OA articles are governed by the applicable Creative Commons License

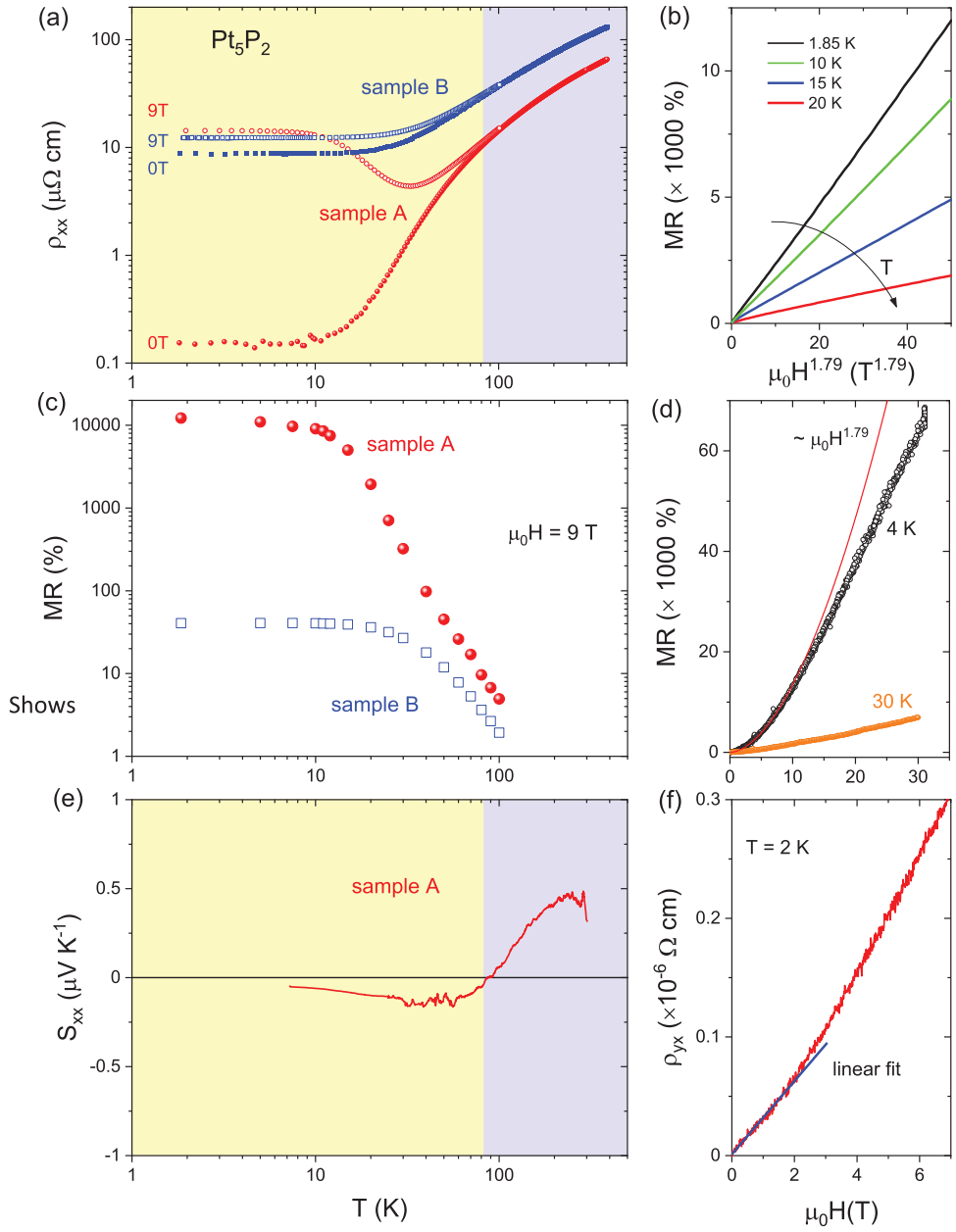

Figure 2. Transport properties of Pt_5P_2. a) Temperature dependence of the resistivity for samples A and B, under $B = 0$ and 9 T. b) MR of sample A measured at multiple fixed temperatures up to 9 T. c) Temperature dependence of the MR for samples A and B. d) MR of sample A measured up to 30 T for $T = 4$ and 30 K. e) Temperature dependence of the Seebeck coefficient, and f) Hall resistivity, both for sample A.

Thus, in such cases, the MR is expected to increase in proportion to the product of the electron and hole mobilities. Since Pt_5P_2 is highly metallic with a large carrier concentration n, it can be assumed that the sample dependence would not largely impact the value of n; hence, we could treat n as an approximately constant across samples with different crystallinity. Therefore, the zero-field conductivity $\sigma(B = 0) = ne\mu \propto \mu$, and by combining this with Equation (1), the MR under a fixed B at a given temperature can be considered to follow the relation:

$$\mathrm{MR}(B = \mathrm{const.}) \sim \mu^2 \propto \sigma(B = 0)^2 \quad (2)$$

As can be seen in Figure 3, the MR observed in this study plotted against the low-T conductivity $\sigma_{T\sim 2\mathrm{K}}{}^{B=0\mathrm{T}}$ reasonably follows this relation, which is depicted as a dotted line. The fitted values obtained in Figures 2b and 3 are consistent with Equations (1) and (2), respectively. Thus, Pt_5P_2 appears to be a relatively well-compensated metal. At high magnetic fields, on the other hand, the MR deviates from quadratic behavior and appears to approach a linear B-dependence (Figure 2d). One model for linear MR in polycrystals is the classical disorder model.[31] However, we conclude that the MR behavior of Pt_5P_2 does not fit the classical disorder model for several reasons.

© 2022 The Authors. Advanced Electronic Materials published by Wiley-VCH GmbH

MOST WIEDZY Downloaded from mostwiedzy.pl
2199160x, 0, Downloaded from https://onlinelibrary.wiley.com/doi/10.1002/aelm.202201120 by Tomasz Klimczuk - Pcp/Technical University Of , Wiley Online Library on [30/12/2022]. See the Terms and Conditions (https://onlinelibrary.wiley.com/terms-and-conditions) on Wiley Online Library for rules of use; OA articles are governed by the applicable Creative Commons License

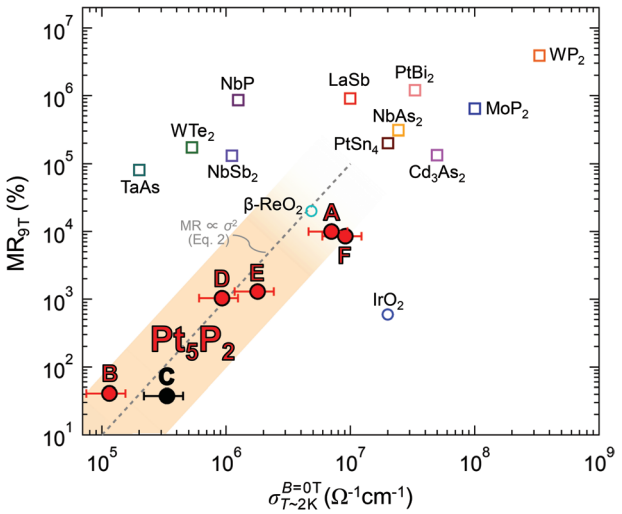

Figure 3. Comparison of MR (≈2 K, 9 T) and low-temperature electrical conductivity σ (≈2 K, 0 T) among well-known metals and semimetals. The data of the materials besides Pt_5P_2 were taken from references.[5,6,8,11,23–30] Metals are denoted by hollow circles, and semimetals by hollow squares. Data for the Pt_5P_2 samples are denoted with red solid circles. The Ir-doped sample C is denoted in black and is distinguished from the rest of the nondoped Pt_5P_2 samples. The plotted data are all for single crystal samples except for Pt_5P_2 samples A–F. The gray-dashed line represents the MR ∝ σ^2 dependence based on Equation (2).

First, by comparing sample A (main sample) and sample C (Ir-doped), one can see that the MR does not increase with increasing disorder. Second, in the classical disorder model, linearity of the MR is expected to appear at extremely low magnetic fields (i.e., $\beta = \mu B < 1$, where β is the product of carrier mobility and magnetic flux density, and thus dimensionless). This is not the case for Pt_5P_2 ($\beta \approx 1$ [m^2 V^{-1} s^{-1}] × 10 [T] > 1). Another possible origin is the involvement of Dirac-like charge carriers,[32–34] which will be discussed later on.

To discuss a possible origin of the large MR in Pt_5P_2, we performed electronic structure calculations, with the results shown in **Figure 4**. Figure 4b shows the presence of metallic Fermi surfaces and the coexistence of electron and hole pockets, which are consistent with the experimental results showing the fairly small Seebeck coefficient and the large carrier density. Based on the computational results, we consider the following three factors for the very large MR. The first factor is, as previously mentioned, carrier compensation, which is one of the well-known factors yielding a nonsaturating MR with a quadratic B dependence. This picture is consistent with the multiple small pockets of both electrons and holes seen across the Fermi level in Figure 4a. The second factor is the presence of "open orbits" in the Fermi surface contours.[35] Open trajectories are also known to yield nonsaturating and quadratic behavior of MR. As seen in Figure 4c near the X-point, the Fermi surface of Pt_5P_2 shows "open orbits" that repeatedly connect to the adjacent Brillouin zone; hence, the carriers' trajectory does not close in the momentum space. Recent theoretical work reveals that the Fermi surface trajectory can be a crucially important mechanism causing the observed MR behavior in many materials.[36] Finally, the presence of a topological nodal-band structure can be viewed as an additional possibility. Even in the presence of spin orbit coupling (SOC), one can see that the band crossing formed at the L-point is preserved. Combined with the proximity of the band crossing to the Fermi level, such Dirac-like dispersion with small effective mass can be considered to contribute to the nonsaturating and linear behavior of the giant MR at high fields.

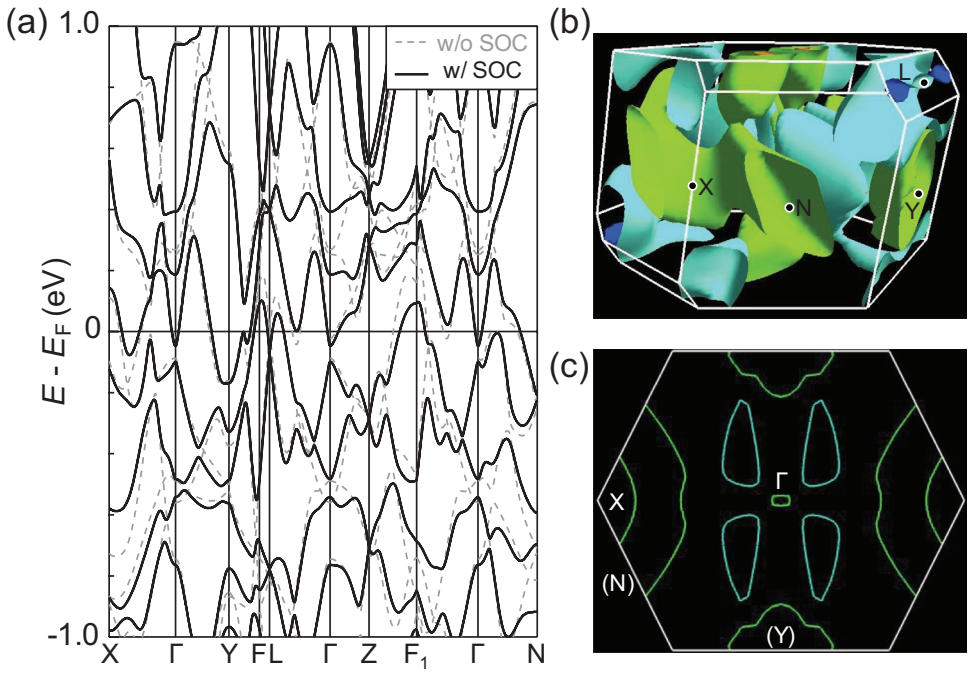

Figure 4. a) Band structure of Pt_5P_2 calculated with (black solid line) and without (gray-dashed line) SOC. b) Calculated Fermi surface of Pt_5P_2 and c) its cross-section projected to the (001) surface in its monoclinic Brillouin zone. It is evident in (c) that there exists an open orbit on the Fermi surface.

© 2022 The Authors. Advanced Electronic Materials published by Wiley-VCH GmbH

MOST WIEDZY Downloaded from mostwiedzy.pl

2199160x, 0, Downloaded from https://onlinelibrary.wiley.com/doi/10.1002/aelm.202201120 by Tomasz Klimczuk - Pcp/Technical University Of , Wiley Online Library on [30/12/2022]. See the Terms and Conditions (https://onlinelibrary.wiley.com/terms-and-conditions) on Wiley Online Library for rules of use; OA articles are governed by the applicable Creative Commons License

3. Conclusion

We have successfully synthesized a series of high-purity polycrystalline Pt_5P_2 samples. The samples were shown to be single phase by powder XRD. The MR measured at 9 T showed an extremely large positive value (10 000%) despite the fact that the materials were in polycrystalline form. Low-temperature heat capacity measurements reveal that the material has a nonzero Sommerfeld parameter, which further confirms the presence of a finite electronic density of states at the Fermi energy level. We have also observed a clear relation between carrier mobility and MR. The calculated electronic structure displays multiple characteristics that could strongly contribute to the very large MR; namely, carrier compensation, open orbits, and Dirac-like nodes near the Fermi level. The fact that the MR and conductivity of polycrystalline Pt_5P_2 are comparable with well-known high-MR single crystals of topological semimetals dramatically extends the landscape of high MR candidates from low-carrier concentration single crystals with simple Fermi surfaces to polycrystalline metals with complicated Fermi surfaces. The MR–σ correlation presented in Figure 3 implies that improvement of the sample purity and crystallinity could further enhance the MR of Pt_5P_2, possibly nearing the record value. It is worth noting that in some cases where Dirac-like bands are involved, there is another possibility, namely that inhomogeneity could favor MR rather than diminish it,[37] which could manifest as a deviation from the MR–σ relation observed here as the crystallinity approaches the single crystalline form.

4. Experimental Section

Pt_5P_2 polycrystalline samples were synthesized in two ways. Stoichiometric powders of elemental Pt (Mennica, Poland, 3N or 4N) and P (Alfa Aesar, 5N+, lumps) were sealed in an evacuated quartz glass tube, heated to 950 °C at a rate of 25 °C h^{-1}, held at that temperature for 5 h and then quenched in a water/ice mixture. Rapid cooling was important in order to avoid the formation of the PtP_2 phase. The material was heated at 570 °C for 2 weeks. This method was used in the synthesis of several samples including stoichiometric Pt_5P_2, marked as sample A in the following. Sample B was made by a typical solid-state reaction method. Stoichiometric powders were ground, pressed into a pellet, and heated in a sealed quartz tube at 570 °C for 4 days. The sample was then ground thoroughly, pressed into a pellet, sealed in a quartz tube, and annealed for another 2 days. A list of the samples and details of the synthesis process were given in the Table S1 (Supporting Information).

Room-temperature powder X-ray diffraction (pXRD) was conducted by using a Bruker D2 Phaser second-generation diffractometer with CuK_α radiation (λ = 1.5404 Å) and XE-T detector. The XRD patterns were analyzed with the Bruker Topas software.

Resistivity measurements were performed using a four-probe technique with thin Pt wires (d = 50 µm) mounted using a spot-welding technique on the surface of a rectangular bar sample. Low-field measurements were performed in an Evercool II Physical Property Measurement System (PPMS Quantum Design) in magnetic fields up to 9 Tesla (T). For high-field measurements, up to 35 T DC, the experiments were conducted at the National High Magnetic Field Laboratory, Tallahassee, FL, USA. The Seebeck coefficient was measured by the steady-state method. The sample was mounted on copper blocks used for the heat-bath and for electrical contacts. The temperature gradient was measured by chromel–constantan thermocouples. The measurement setup was installed into a cryostat (Pascal Co., Ltd., Japan). A FEI Quanta 250 FEG scanning electron microscope, under high-vacuum conditions with electron energy set to 20 or 30 keV was used to image the sample surface.

Relativistic and nonrelativistic bulk electronic structure calculations were performed within density functional theory using the Perdew–Burke–Ernzerhof (PBE) exchange-correlation functional[38] as implemented in the Quantum ESPRESSO code.[39–41] The projector augmented wave (PAW) method was used to account for the treatment of core electrons.[42] The cutoff energy for plane waves forming the basis set was set to 60 Ry. The lattice parameters and atomic positions were taken from the single-crystal XRD experiment. The Brillouin zone was sampled by a 12 × 12 × 12 *k*-mesh for the PWscf calculation and a 36 × 36 × 36 *k*-mesh for the Fermi surface visualization via the FermiSurfer package.[43] Crystal structures were visualized using VESTA.[44]

Supporting Information

Supporting Information is available from the Wiley Online Library or from the author.

Acknowledgements

The work at Gdansk Tech. was supported by the National Science Centre (Poland; grant No. 2018/30/M/ST5/00773). The work at Princeton was supported by the Gordon and Betty Moore Foundation (grant No. GBMF-9066), and by the DOE- BES-funded Co-design Center for Quantum Advantage (grant No. DE-SC0012704). The work at MSU was supported by Beckman Young Investigator Award. The work at Osaka was supported by JSPS, KAKENHI (grant Nos. 21H01030 and 22H00343), and Murata Foundation. The part performed at NHMFL has been supported by NSF DMR-1644779 and the State of Florida. A.H.M. was supported by the Program for Leading Graduate Schools "World-leading Innovative Graduate Study Program for Materials Research, Industry and Technology (MERIT-WINGS)" of the University of Tokyo.

Conflict of Interest

The authors declare no conflict of interest.

Data Availability Statement

The data that support the findings of this study are available from the corresponding author upon reasonable request.

Keywords

giant magnetoresistance, magnetotransport measurements, polycrystalline compounds, thermoelectric measurements

Received: October 6, 2022
Revised: November 16, 2022
Published online:

[1] R. Xu, A. Husmann, T. F. Rosenbaum, M.-L. Saboungi, J. E. Enderby, P. B. Littlewood, *Nature* **1997**, *390*, 57.
[2] Z. Ogorelec, A. Hamzić, M. Basletić, *Europhys. Lett.* **1999**, *46*, 56.
[3] S. Cho, Y. Kim, L. J. Olafsen, I. Vurgaftman, A. J. Freeman, G. K. L. Wong, J. R. Meyer, C. A. Hoffman, J. B. Ketterson, *J. Magn. Magn. Mater.* **2002**, *239*, 201.
[4] S. Ishiwata, Y. Shiomi, J. S. Lee, M. S. Bahramy, T. Suzuki, M. Uchida, R. Arita, Y. Taguchi, Y. Tokura, *Nat. Mater.* **2013**, *12*, 512.

© 2022 The Authors. Advanced Electronic Materials published by Wiley-VCH GmbH

MOST WIEDZY Downloaded from mostwiedzy.pl

2199160x, 0, Downloaded from https://onlinelibrary.wiley.com/doi/10.1002/aelm.202201120 by Tomasz Klimczuk - Pcp/Technical University Of , Wiley Online Library on [30/12/2022]. See the Terms and Conditions (https://onlinelibrary.wiley.com/terms-and-conditions) on Wiley Online Library for rules of use; OA articles are governed by the applicable Creative Commons License

[5] M. N. Ali, J. Xiong, S. Flynn, J. Tao, Q. D. Gibson, L. M. Schoop, T. Liang, N. Haldolaarachchige, M. Hirschberger, N. P. Ong, R. J. Cava, *Nature* **2014**, *514*, 205.
[6] C. Shekhar, A. K. Nayak, Y. Sun, M. Schmidt, M. Nicklas, I. Leermakers, U. Zeitler, Y. Skourski, J. Wosnitza, Z. Liu, Y. Chen, W. Schnelle, H. Borrmann, Y. Grin, C. Felser, B. Yan, *Nat. Phys.* **2015**, *11*, 645.
[7] P. Kapitza, *Proc. R. Soc. Lond. Series A* **1928**, *119*, 358.
[8] D. Hirai, T. Anbai, S. Uji, T. Oguchi, Z. Hiroi, *J. Phys. Soc. Jpn.* **2021**, *90*, 094708.
[9] W. Liu, Z. Wang, J. Wang, H. Bai, Z. Li, J. Sun, X. Zhou, J. Luo, W. Wang, C. Zhang, J. Wu, Y. Sun, Z. Zhu, Q. Zhang, X. Tang, *Adv. Funct. Mater.* **2022**, *32*, 2202143.
[10] M. N. Ali, L. Schoop, J. Xiong, S. Flynn, Q. Gibson, M. Hirschberger, N. P. Ong, R. J. Cava, *EPL* **2015**, *110*, 67002.
[11] K. Yokoi, H. Murakawa, M. Komada, T. Kida, M. Hagiwara, H. Sakai, N. Hanasaki, *Phys. Rev. Mater.* **2018**, *2*, 024203.
[12] E. Dahl, G. Ahnström, T. Ledaal, P. Holmberg, G. Eriksson, R. Blinc, S. Paušak, L. Ehrenberg, J. Dumanović, *Acta Chem. Scand.* **1967**, *21*, 1131.
[13] M. Ellner, M. El-Boragy, *J. Alloys Compd.* **1992**, *184*, 131.
[14] L.-O. Gullman, *J. Less-Common Met.* **1966**, *11*, 157.
[15] J. W. Edwards, R. Speiser, H. L. Johnston, *J. Appl. Phys.* **1951**, *22*, 424.
[16] R. Pöttgen, W. Hönle, H. G. von Schnering, in *Encyclopedia of Inorganic and Bioinorganic Chemistry*, John Wiley & Sons, Ltd., New York **2006**.
[17] Q. Xu, R. Yu, Z. Fang, X. Dai, H. Weng, *Phys. Rev. B* **2017**, *95*, 045136.
[18] G. Wang, G. Chang, H. Zhou, W. Ma, H. Lin, M. Z. Hasan, S.-Y. Xu, S. Jia, *Chin. Phys. Lett.* **2020**, *37*, 107501.
[19] A. H. Mayo, J. A. Richards, H. Takahashi, S. Ishiwata, *J. Phys. Soc. Jpn.* **2021**, *90*, 123704.
[20] A. H. Mayo, H. Takahashi, M. S. Bahramy, A. Nomoto, H. Sakai, S. Ishiwata, *Phys. Rev. X* **2022**, *12*, 011033.
[21] W. Wu, Z. H. Yu, M. Xu, X. L. Liu, J. G. Zhao, Z. Y. Liu, W. Xia, Z. Y. Li, C. Y. Zhou, J. J. Feng, M. Xu, Y. F. Guo, J. L. Luo, *Appl. Phys. A: Mater. Sci. Process.* **2022**, *128*, 196.
[22] G. Eguchi, S. Paschen, *Phys. Rev. B* **2019**, *99*, 165128.
[23] W. D. Ryden, W. A. Reed, E. S. Greiner, *Phys. Rev. B* **1972**, *6*, 2089.
[24] E. Mun, H. Ko, G. J. Miller, G. D. Samolyuk, S. L. Bud'ko, P. C. Canfield, *Phys. Rev. B* **2012**, *85*, 035135.
[25] K. Wang, D. Graf, L. Li, L. Wang, C. Petrovic, *Sci. Rep.* **2014**, *4*, 7328.
[26] X. Huang, L. Zhao, Y. Long, P. Wang, D. Chen, Z. Yang, H. Liang, M. Xue, H. Weng, Z. Fang, X. Dai, G. Chen, *Phys. Rev. X* **2015**, *5*, 031023.
[27] T. Liang, Q. Gibson, M. N. Ali, M. Liu, R. J. Cava, N. P. Ong, *Nat. Mater.* **2015**, *14*, 280.
[28] F. F. Tafti, Q. D. Gibson, S. K. Kushwaha, N. Haldolaarachchige, R. J. Cava, *Nat. Phys.* **2015**, *12*, 272.
[29] W. Gao, N. Hao, F.-W. Zheng, W. Ning, M. Wu, X. Zhu, G. Zheng, J. Zhang, J. Lu, H. Zhang, C. Xi, J. Yang, H. Du, P. Zhang, Y. Zhang, M. Tian, *Phys. Rev. Lett.* **2017**, *118*, 256601.
[30] N. Kumar, Y. Sun, N. Xu, K. Manna, M. Yao, V. Süss, I. Leermakers, O. Young, T. Förster, M. Schmidt, H. Borrmann, B. Yan, U. Zeitler, M. Shi, C. Felser, C. Shekhar, *Nat. Commun.* **2017**, *8*, 1642.
[31] M. M. Parish, P. B. Littlewood, *Nature* **2003**, *426*, 162.
[32] A. A. Abrikosov, *Phys. Rev. B* **1998**, *58*, 2788.
[33] A. A. Abrikosov, *Europhys. Lett.* **2000**, *49*, 789.
[34] M. Owada, Y. Awashima, Y. Fuseya, *J. Phys.: Condens. Matter* **2018**, *30*, 445601.
[35] J. M. Ziman, *Principles of the Theory of Solids*, Cambridge University Press, Cambridge, UK **1972**.
[36] S. Zhang, Q. Wu, Y. Liu, O. V. Yazyev, *Phys. Rev. B* **2019**, *99*, 035142.
[37] J. Hu, T. F. Rosenbaum, *Nat. Mater.* **2008**, *7*, 697.
[38] J. P. Perdew, K. Burke, M. Ernzerhof, *Phys. Rev. Lett.* **1996**, *77*, 3865.
[39] P. Giannozzi, S. Baroni, N. Bonini, M. Calandra, R. Car, C. Cavazzoni, D. Ceresoli, G. L. Chiarotti, M. Cococcioni, I. Dabo, A. Dal Corso, S. de Gironcoli, S. Fabris, G. Fratesi, R. Gebauer, U. Gerstmann, C. Gougoussis, A. Kokalj, M. Lazzeri, L. Martin-Samos, N. Marzari, F. Mauri, R. Mazzarello, S. Paolini, A. Pasquarello, L. Paulatto, C. Sbraccia, S. Scandolo, G. Sclauzero, A. P. Seitsonen, et al., *J. Phys.: Condens. Matter* **2009**, *21*, 395502.
[40] P. Giannozzi, O. Andreussi, T. Brumme, O. Bunau, M. Buongiorno Nardelli, M. Calandra, R. Car, C. Cavazzoni, D. Ceresoli, M. Cococcioni, N. Colonna, I. Carnimeo, A. Dal Corso, S. de Gironcoli, P. Delugas, R. A. DiStasioJr, A. Ferretti, A. Floris, G. Fratesi, G. Fugallo, R. Gebauer, U. Gerstmann, F. Giustino, T. Gorni, J. Jia, M. Kawamura, H.-Y. Ko, A. Kokalj, E. Küçükbenli, M. Lazzeri, et al., *J. Phys.: Condens. Matter* **2017**, *29*, 465901.
[41] Quantum Espresso, http://www.quantum-espresso.org (accessed: July 2022).
[42] A. Dal Corso, *Comput. Mater. Sci.* **2014**, *95*, 337.
[43] M. Kawamura, *Comput. Phys. Commun.* **2019**, *239*, 197.
[44] K. Momma, F. Izumi, *J. Appl. Crystallogr.* **2011**, *44*, 1272.

MOST WIEDZY Downloaded from mostwiedzy.pl

© 2022 The Authors. Advanced Electronic Materials published by Wiley-VCH GmbH

2199160x, 0, Downloaded from https://onlinelibrary.wiley.com/doi/10.1002/aelm.202201120 by Tomasz Klimczuk - Pcp/Technical University Of , Wiley Online Library on [30/12/2022]. See the Terms and Conditions (https://onlinelibrary.wiley.com/terms-and-conditions) on Wiley Online Library for rules of use; OA articles are governed by the applicable Creative Commons License